Supporting Information for

Hidden Charge Order and Multiple Electronic Instabilities in $EuTe_4$

Kebin Xiao[1,2]†, Wen-Han Dong[1,2]†, Xintong Wang[1,2]†, Jiawei Yu[1,2]†, Daran Fu[1,2], Zhiqiang Hu[1,2], Yunkai Guo[1,2], Qinqin Zhang[1,2], Xiaofei Hou[3], Yanfeng Guo[3,4], Lexian Yang[1,2], Yong Xu[1,2], Peizhe Tang[5,6], Wenhui Duan[1,2], Qikun Xue[1,2,7,8]*, and Wei Li[1,2]**

[1]State Key Laboratory of Low-Dimensional Quantum Physics, Department of Physics, Tsinghua University, Beijing 100084, China;

[2]Frontier Science Center for Quantum Information, Beijing 100084, China;

[3]School of Physical Science and Technology, ShanghaiTech University, Shanghai 201210, China;

[4]ShanghaiTech Laboratory for Topological Physics, ShanghaiTech University, Shanghai 201210, China;

[5]School of Materials Science and Engineering, Beihang University, Beijing 100191, People's Republic of China;

[6]Max Planck Institute for the Structure and Dynamics of Matter, Center for Free Electron Laser Science, 22761 Hamburg, Germany;

[7]Beijing Academy of Quantum Information Sciences, Beijing 100193, China;

[8]Southern University of Science and Technology, Shenzhen 518055, China

*To whom correspondence should be addressed: weili83@tsinghua.edu.cn; qkxue@mail.tsinghua.edu.cn; peizhet@buaa.edu.cn.

Contents

Supplementary Note 1: DFT Simulations on STM Image 3
Supplementary Note 2: Bias Dependence of the Stripe-like Charge Order 5
Supplementary Note 3: Rotation of the Stripe-like Charge Order 7
Supplementary Note 4: Generic Discussions for Wave Vector Mixing 9
Supplementary Note 5: Origin of the Two Types of CDW States 11
Supplementary Note 6: Reasonable explanation for the 90° rotation of stripe CDW 14
Supplementary Note 7: Bias Dependence of the Spindle-shaped Charge Order 15
Supplementary Note 8: Rotation of the Spindle-shaped Charge Order 17
Supplementary Note 9: The Stripe-like Charge Order at 77 K 19
References 20

Supplementary Note 1: DFT Simulations on STM Image

We applied the DFT calculations to simulate the STM image for $EuTe_4$ with and without the CDW. As shown in Fig. 1a and Fig. S1, we distinguish the Te atoms into (i) Te-1 atoms; and (ii) Te-2 atoms, which form dimers along $\boldsymbol{c}$ direction. For the high temperature (HT) phase without CDW order, we discover that the "bright" local density of states (LDOS) are contributed by Te-1 atoms, and the DOS contributions from Te-2 atoms are low, corresponding to the "dark" sites. The lattice contributed by the "bright" sites corresponds to the FFT peaks at $\boldsymbol{q} = \boldsymbol{b}_1$, which is consistent with our experiments. When forming the CDW order within 1×3×1-supercell, such brightness of Te-1 atoms still can be observed (see Fig. S1b), although its pattern is modulated along $\boldsymbol{b}$ axis to form a stripe-like CDW order.

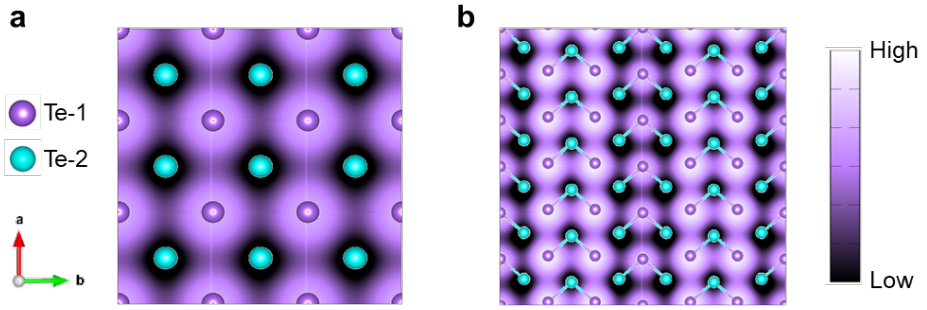

Fig. S1. STM simulations at V = -1 V of (a) HT $EuTe_4$, and (b) stripe-CDW reconstructed $EuTe_4$.

To understand such effect, we calculate the electronic structure for $EuTe_4$ at HT phase without CDW. Figure S2 shows the band structures and density of state (DOS) projected on atomic orbitals of surface Te atoms. Around the Fermi level, the metallic bands are mainly contributed by the $p_{x,y}$ orbital of Te atoms. For the p_z orbitals of Te atoms that contribute largely for the tunnelling currents and are easier to be detected by STM, their contribution is relatively small. Due to the formation of Te-2 dimer, the p_z orbitals of Te-2 atoms form the bonding and anti-bonding states away from the Fermi level (see Fig. S2c). While p_z orbitals of Te-1 atoms are relatively localized closed to the Fermi level, i.e., [-2.6 eV, -0.6 eV]. Consequently, the DOS localized on Te-1 atoms are brighter than that on Te-2 atoms in STM if the V_{bias} is around -1 V, so that the $\boldsymbol{q} = \boldsymbol{b_1}$ peak is obvious.

If the applied bias in STM measurement is closer to Fermi level (e.g., V_{bias} = -0.2 V), the influence of p_z orbitals to LDOS can be neglected (see Fig. S2). At this time, Te-1 and Te-2 have similar contributions (from $p_{x,y}$ orbitals) to the measured STM, which induces the decrease of FFT strength at $\boldsymbol{q} = \boldsymbol{b_1}$, but an increasing FFT strength at another $\boldsymbol{q} = \boldsymbol{q}_{\mathbf{Te}}$ ($|\boldsymbol{q}_{\mathbf{Te}}| \approx \sqrt{2}|\boldsymbol{b_1}|$). It explains why our experiments also observed notable FFT peak at $\boldsymbol{q} = \boldsymbol{q}_{\mathbf{Te}}$ when V_{bias} is closer to 0 V (see Fig. S3).

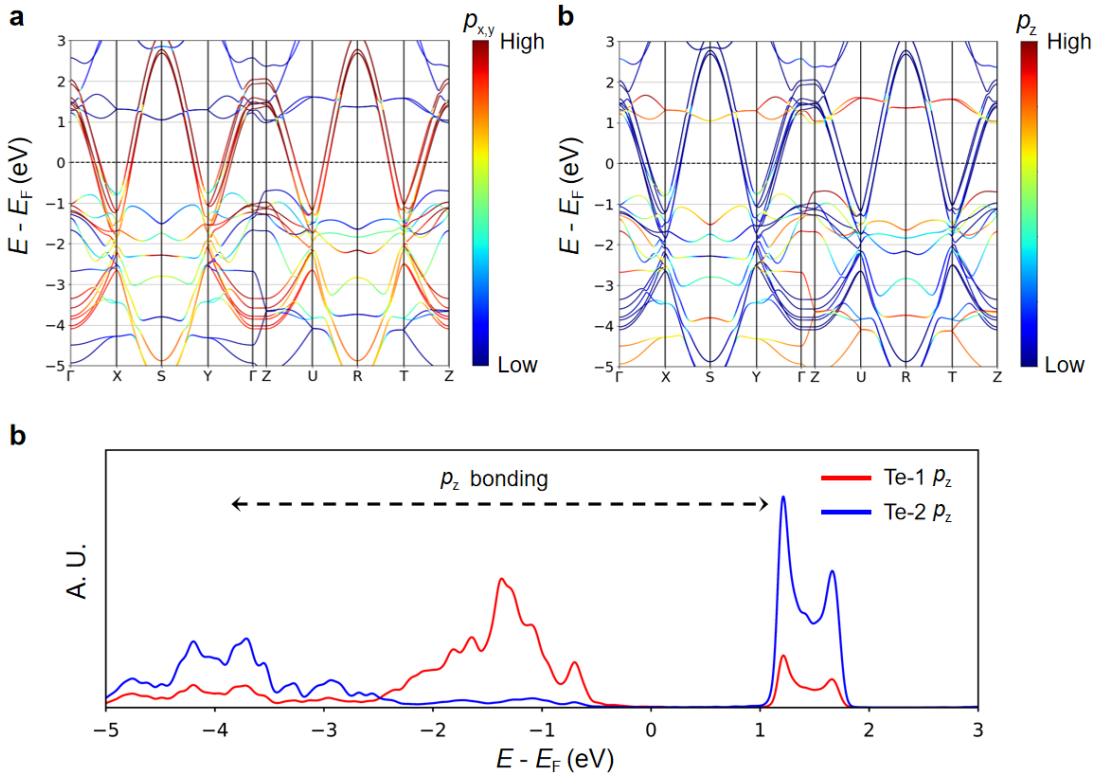

Fig. S2. Projected bands of HT $EuTe_4$ into (a) $p_{x,y}$ orbitals and (b) p_z orbitals. (c) Projected DOS of HT $EuTe_4$ into p_z orbital of Te-1 (red) and p_z orbital of Te-2 (blue).

Supplementary Note 2: Bias Dependence of the Stripe-like Charge Order

Figure S3a-c exhibit the STM images measured on the same area of the sample with different bias voltages. As indicated by the FFT in Fig. S3d-f, the relative intensity between $\boldsymbol{b}_1$ and $\boldsymbol{q}_{Te}$ varies with bias voltages, where $\boldsymbol{b}_1$ arises from the lattice of surface Te-1 atoms and $\boldsymbol{q}_{Te}$ comes from the joint contributions from Te-1 atoms and Te-2 atoms. We found $\boldsymbol{q}_{Te}$ becomes obvious when the applied voltage is close to 0 V, which is consistent with our calculations in Supplementary Note 1. In Fig. S3g, a series of bias-dependent FFT line-cuts shows the intensities of $\boldsymbol{q}_1$, $\boldsymbol{q}_2$ and $\boldsymbol{q}_3$ are changing with the intensity of $\boldsymbol{b}_1$ under different voltages, while intensity of $\boldsymbol{q}_0$ hardly changes. Thus, the bias manipulation of strength of lattice vectors could be utilized for tuning the strength of satellite peaks, see discussions in Supplementary Note 4 below.

Figure S4 exhibit the FFT images of bias-dependent differential conductance mappings of the stripe-like charge order. $\boldsymbol{q}_1$, $\boldsymbol{q}_2$, $\boldsymbol{q}_3$ and $\boldsymbol{q}_0$ show no frequency shift at different biases.

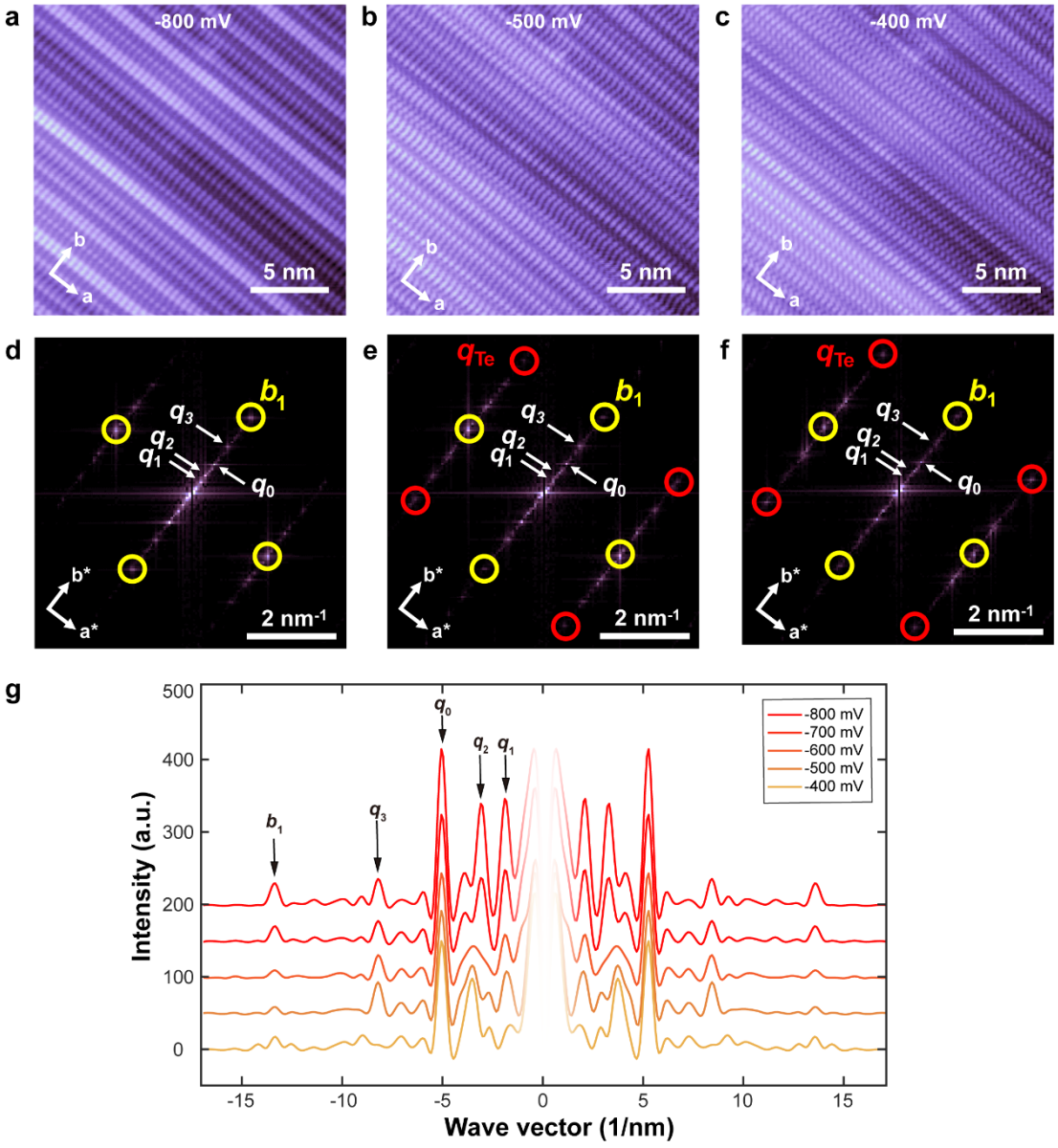

Fig. S3. Bias dependence of the stripe-like charge order. (a-c) STM images taken on the same area with different bias voltages (at 4 K, 20 nm × 20 nm; V_b = -800, -500 and -400 mV, respectively; I_t = 100 pA). (d-f) FFT of (a-c). (g) A series of FFT line-cuts of the STM images under different biases along $\boldsymbol{b}_1$ direction.

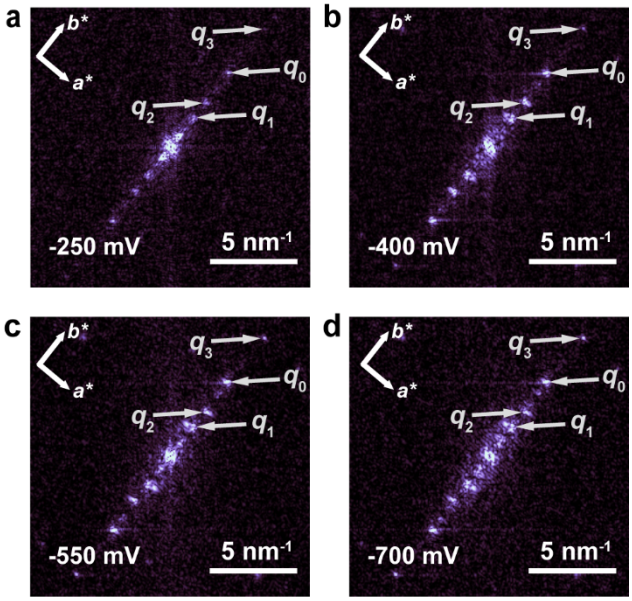

Fig. S4. FFT images of dI/dV mapping of the stripe-like charge order at different biases (at 4 K; set point: V_b = -1 V; I_t = 200 pA).

Supplementary Note 3: Rotation of the Stripe-like Charge Order

We notice the orientation of the stripe-like charge order can rotate 90°, i.e., rotating from the (long) ***b*** axis to the (short) ***a*** axis in certain regions (see Fig. S5a and b). For better comparison, we count the ratio of stripe-like charge order along ***a***-axis to that along ***b***-axis is approximate about 1:9. The resulting $\boldsymbol{q}_0$, $\boldsymbol{q}_1$ $\boldsymbol{q}_2$ and $\boldsymbol{q}_3$ (Fig. S5b and c) can also be observed, similar with those observed in the regions with the CDW order along the $\boldsymbol{b}^*$ axis (Fig. 2b and c). We found the lattice changes slightly in the region with the rotated stripe-like charge order, in which the lattice constants become $a = 4.53$ Å, $b = 4.63$ Å in contrast to those with $\boldsymbol{q}_0$ along $\boldsymbol{b}^*$ axis ($a = 4.50$ Å, $b = 4.67$ Å). The previous research of $R\mathrm{Te}_3$ indicates that the formation of CDW should stretch the lattice along the direction of CDW modulations, while compress the lattice in the perpendicular direction.[1] In a similar way, our observations in Fig. S5 suggest that once the CDW modulations are along the direction with smaller lattice constant (***a*** axis), the lattice constant difference between ***a*** and ***b*** axis decreases. Notice though there is a recent study that claims to have observed the ***a***-axis CDW of EuTe_4, its strength is orders of magnitude weaker than ***b***-axis CDW.[2] In comparison, the observed ***a***-axis CDW have comparable strength and same ***q***-length with that of ***b***-axis CDW (see Fig. S5d), indicating the strong competitions between the stripe CDWs along two orthorhombic directions. The dI/dV spectra measured in the two regions with different stripe orientations did not show significant differences. Besides, as compared with the stripe-like order along the ***b*** axis (Fig. 2a), more defects can be observed in the regions with the CDW order along the ***a*** axis (Fig. S5a).

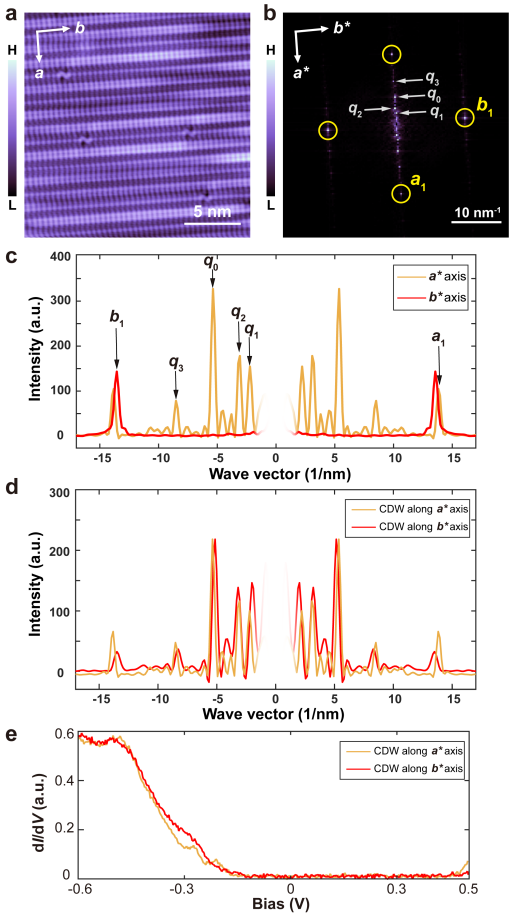

Figure S5. Stripe-like charge order with its orientation rotated 90°. (a) STM image of stripe-like charge order along ***a*** axis (20 nm × 20 nm, V_b = -800 mV, I_t = 200 pA). (b) FFT of (a). The wavevectors related with CDW is along the direction with smaller lattice constant (***a**** axis). (c) Line-cuts of (b) along $\boldsymbol{a}_1$ and $\boldsymbol{b}_1$ directions. (d) The ***q***-length comparison when the stripe CDW is along the $\boldsymbol{a}_1$ and $\boldsymbol{b}_1$ directions. The red line originates from Figure 2c, while the yellow line is derived from Figure S5c and has been contracted to facilitate a more effective comparison. (e) dI/dV spectra (V_b = -800 mV, I_t = 200 pA) taken in the two regions with different stripe CDW orientations.

Supplementary Note 4: Generic Discussions for Wave Vector Mixing

To understand the appearance of multiple $\boldsymbol{q}$ in FFT image, we study the wave vector mixing[3] for incommensurate CDW (ICCDW) observed in $EuTe_4$. We begin with the simple 1D case hosting two wake-like quantum states, the superposition of their wave functions is written as:

$$\psi(x) = u_1 e^{iQ_1 x} + u_2 e^{iQ_2 x} + \mathrm{C}_1(x), \tag{S1}$$

Where $u_{1,2}$ are amplitudes of two waves, $Q_{1,2}$ are wave vectors (supposing $Q_2 < Q_1$), and $\mathrm{C}_1(x)$ is the background as function of position x. Considering the incommensurate situations $Q_1 \neq nQ_2$, note that there exists peak-valley asymmetry between two waves (see Fig. S6). Such asymmetry is reflected as the coupling terms of two waves in the observables like STM signal. If we perform the measurement on this 1D system, the detected STM signal, i.e., $S(x)$, should be expanded as:

$$\begin{aligned} S(x) = \mathrm{C}_2(x) &+ \sum_{n=1}^{\infty} (b_{1n} \sin(nQ_2 x) + b_{2n} \cos(nQ_2 x)) \\ &+ \sum_{n=1}^{\infty} (b_{3n} \sin(nQ_1 x) + b_{4n} \cos(nQ_1 x)) \\ &+ \sum_{\substack{n=1, \\ m=1}}^{\infty} (d_{11}^{nm} \sin(nQ_2 x) \sin(mQ_1 x) + d_{12}^{nm} \sin(nQ_2 x) \cos(mQ_1 x)) \\ &+ d_{21}^{nm} \cos(nQ_2 x) \sin(mQ_1 x) \\ &+ d_{22}^{nm} \cos(nQ_2 x) \cos(mQ_1 x)), \end{aligned} \tag{S2}$$

where $\mathrm{C}_2(x)$ is the position-dependent background, b_{in} and d_{ij}^{mn} corresponding to the coefficients of FFT signals for individual terms and couplings terms, respectively. Based on Eq. (S2), the satellite peaks in the FFT signals emerge naturally due to the coupling terms between Q_1 and Q_2. For example, the $\sin(Q_1 x)\sin(Q_2 x)$ terms give rise to two FFT peaks at $\boldsymbol{q} = Q_1 - Q_2$ and $\boldsymbol{q} = Q_1 + Q_2$. The $Q_1 - Q_2$ and $Q_1 + Q_2$ peaks are satellite peaks from the first-order asymmetry-induced coupling. In this sense, such effect from the superposition of two incommensurate waves is known as wave vector mixing.

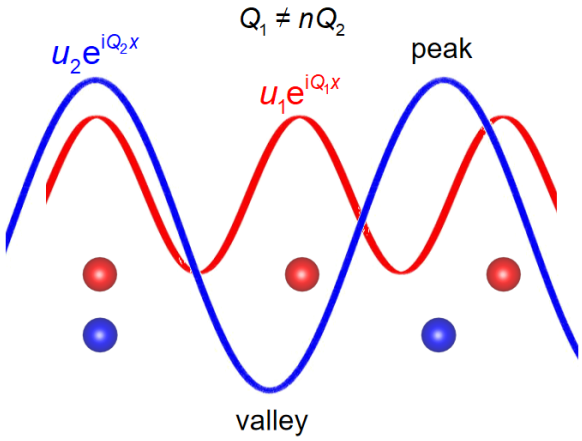

Fig. S6. Schematic for the superposition of two waves with incommensurate periods, in which peak-valley asymmetry exists.

As for the incommensurate stripe-like CDW of $EuTe_4$, our STM signal $S(x)$ mainly composes of the lattice vector $Q_1 = \boldsymbol{b_1}$ from the patterns contributed by Te-1 atoms, and $Q_2 = \boldsymbol{q_0} \approx 0.38\boldsymbol{b_1}$ from the dominant CDW modulation. Considering the mirror symmetry ($\mathcal{M}$) which performs as: $\mathcal{M}|\psi(x)\rangle = |\psi(-x)\rangle$, we obtain the restriction $S(x) = S(-x)$ because $\mathcal{M}^2 = 1$. It ensures the intensities at **q** and -**q** are equivalent, as also seen in Fig. S3g. Based on Eq. (S2), we now consider the STM signal as follows:

$$S(x) = \mathrm{C}_2(x) + b_{21}\cos(\boldsymbol{q_0}x) + b_{22}\cos(2\boldsymbol{q_0}x) + b_{23}\cos(3\boldsymbol{q_0}x) + b_{41}\cos(\boldsymbol{b_1}x) + d_{11}^{11}\sin(\boldsymbol{q_0}x)\sin(\boldsymbol{b_1}x) + d_{22}^{11}\cos(\boldsymbol{q_0}x)\cos(\boldsymbol{b_1}x) + d_{11}^{21}\sin(2\boldsymbol{q_0}x)\sin(\boldsymbol{b_1}x) + d_{22}^{21}\cos(2\boldsymbol{q_0}x)\cos(\boldsymbol{b_1}x) + d_{11}^{31}\sin(3\boldsymbol{q_0}x)\sin(\boldsymbol{b_1}x) + d_{22}^{31}\cos(3\boldsymbol{q_0}x)\cos(\boldsymbol{b_1}x) + \ldots\ldots \quad \text{(S3)}$$

The positive $\boldsymbol{q}$-values of FFT peaks and their intensities are:

$$0\text{: }\mathrm{C}_2(x), \quad \boldsymbol{q_0}\text{: }b_{21}, \quad 2\boldsymbol{q_0}\text{: }b_{22}, \quad 3\boldsymbol{q_0}\text{: }b_{23}, \quad \boldsymbol{b_1}\text{: }b_{41},$$
$$\boldsymbol{b_1} - \boldsymbol{q_0}\text{: }\frac{1}{2}(d_{11}^{11} + d_{22}^{11}), \quad \boldsymbol{b_1} + \boldsymbol{q_0}\text{: }\frac{1}{2}(d_{22}^{11} - d_{11}^{11}),$$
$$\boldsymbol{b_1} - 2\boldsymbol{q_0}\text{: }\frac{1}{2}(d_{11}^{21} + d_{22}^{21}), \quad \boldsymbol{b_1} + 2\boldsymbol{q_0}\text{: }\frac{1}{2}(d_{22}^{21} - d_{11}^{21}),$$
$$3\boldsymbol{q_0} - \boldsymbol{b_1}\text{: }\tfrac{1}{2}(d_{11}^{31} + d_{22}^{31}), \quad \boldsymbol{b_1} + 3\boldsymbol{q_0}\text{: }\tfrac{1}{2}(d_{22}^{31} - d_{11}^{31}). \quad \text{(S4)}$$

For the coupling terms, the peaks at $\boldsymbol{q_1} = 3\boldsymbol{q_0} - \boldsymbol{b_1} \approx 0.14\boldsymbol{b_1}$, $\boldsymbol{q_2} = \boldsymbol{b_1} - 2\boldsymbol{q_0} \approx 0.24\boldsymbol{b_1}$ and $\boldsymbol{q_3} = \boldsymbol{b_1} - \boldsymbol{q_0} \approx 0.62\boldsymbol{b_1}$ are prominent in our experiment (see Fig. S3g). One should notice the intensities of FFT peaks depend on several factors, such as the applied bias, condition of STM tip, and surface strain/distortion/defect, etc.

Supplementary Note 5: Origin of the Two Types of CDW States

Herein, we calculate electronic susceptibility for $EuTe_4$ without and with stripe CDW to explore the origin of two types of CDW. Typically, the real part of susceptibility, i.e., $\chi'(\mathbf{q})$, is known as Lindhard function. The imaginary part of susceptibility, i.e., $\chi''(\mathbf{q})$, reflects the Fermi surface nesting.[4]

For $\chi'(\mathbf{q})$ of HT phase $EuTe_4$ as shown in Fig. 4e of the main text, we can find a strong but diffuse nesting peak at $q_{\text{stripe}} \approx (0, 0.32)$, which agrees with previous calculations [5]. Figure S7 shows the phonon dispersions of HT phase $EuTe_4$ with the imaginary frequencies. Within $\boldsymbol{q} = 0.35\boldsymbol{b}^*$, the largest negative frequency can be observed. Meanwhile, we could also find a large negative frequency within $\boldsymbol{q} = 0.35\boldsymbol{a}^*$. The momentum $\boldsymbol{q}$ of these two phonon modes are close to positions of nesting peaks shown in Fig. 4e, indicating the stripe-like charge order is likely to be induced by electron-phonon interaction. In Fig. S8, we marked these two nesting wavevectors on the Fermi surface.

In Fig. 4g of the main text and Fig. S10, we show the $\chi'(\mathbf{q})$ of $EuTe_4$ with stripe-CDW is highly temperature-dependent as compared with that of HT phase. In particular, a strong $\boldsymbol{q}_{\text{off-axis}} = (0.027,0)$ is prominent at ultralow temperature. Since $\boldsymbol{q}_{\text{off-axis}}$ is perpendicular to the $\boldsymbol{b}$ axis, the spindle-shaped CDW will appear based on stripe-like CDW at low temperature. We marked $q_{\text{off-axis}}$ on the Fermi surface of $EuTe_4$ with stripe-CDW, as shown in Fig. S9.

In contrast to the nesting peaks of $\chi'(\mathbf{q})$, no obvious peak of $\chi''(\mathbf{q})$ can be found (see Fig. S11). Thus, we conclude both the stripe-like CDW and spindle-shaped CDW originates from the electron-phonon-interaction-induced nesting, instead of pure electronic effects from Fermi surface nesting.

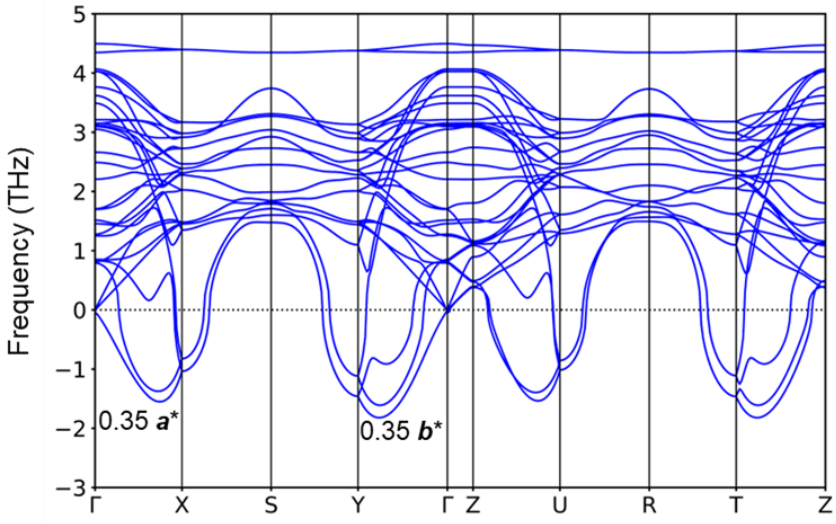

Fig. S7. Phonon dispersions of HT phase $EuTe_4$. Notice the two instabilities emerging at $\mathbf{q} = 0.35\boldsymbol{a}^*$ and $\mathbf{q} = 0.35\boldsymbol{b}^*$, where $\mathbf{q} = 0.35\boldsymbol{b}^*$ exhibits the largest negative frequency.

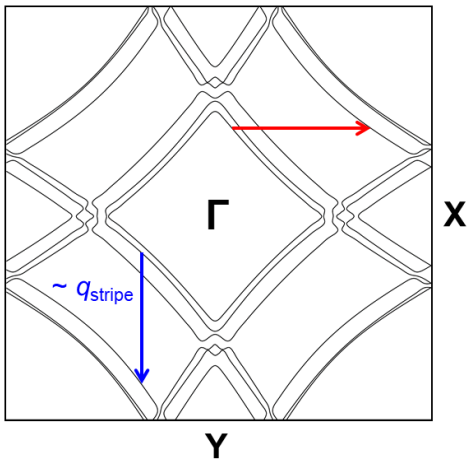

Fig. S8. Fermi surface at $k_z = 0$ plane of HT phase $EuTe_4$. The arrows indicate the nesting peaks as observed in Fig. 4e.

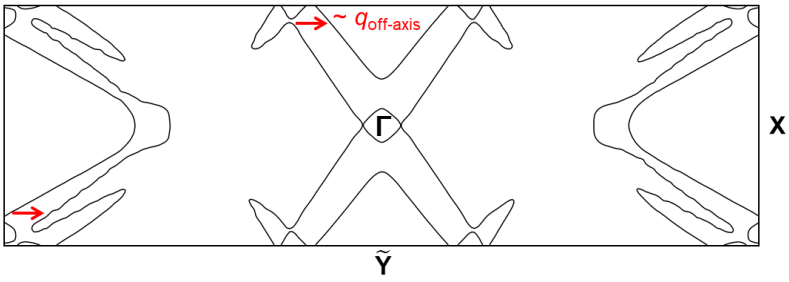

Fig. S9. Fermi surface at $k_z = 0$ plane of stripe-CDW reconstructed $EuTe_4$. The arrows indicate the nesting peak as observed in Fig. 4f.

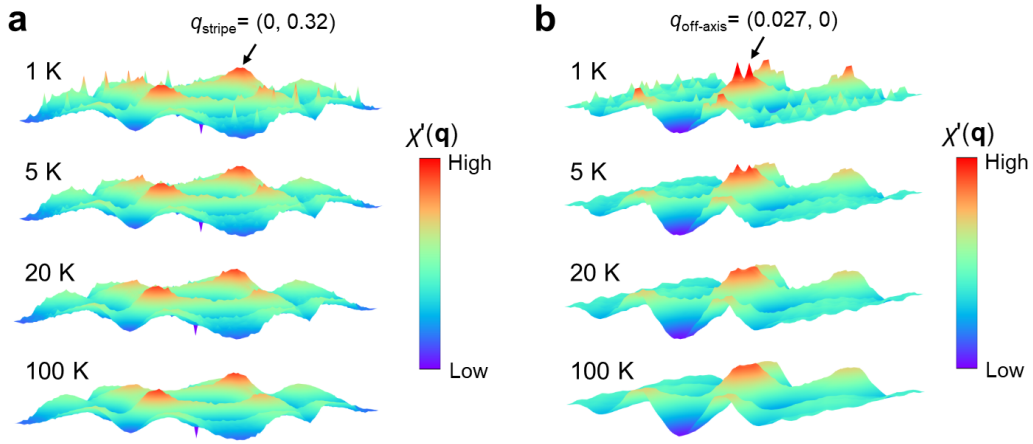

Fig. S10. 3D views of the temperature-dependent $\chi'(\mathbf{q}, T)$ of (a) HT phase $EuTe_4$, and (b) stripe-CDW reconstructed $EuTe_4$.

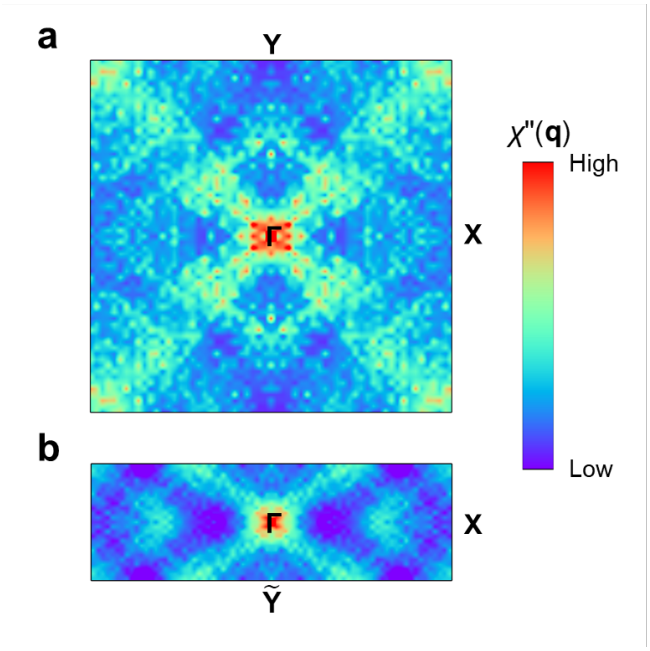

Fig. S11. Imaginary part of the susceptibility ($\chi''(\mathbf{q})$) for (a) HT phase, and (b) stripe-CDW reconstructed phase. Notice the peaks at Γ point are irrelevant to the Fermi surface nesting.

Supplementary Note 6: Reasonable explanation for the 90° rotation of stripe CDW

From DFT, we explain the 90° rotation of stripe CDW in these two aspects. On one hand, the Lindhard function shows Old

nesting peaks in both Γ-X and Γ-Y directions (see Fig. S12), and the value of the peak along ***b***-axis is larger than that along ***a***-axis, which indicates that both ***a***-axial stripe CDW or ***b***-axial stripe CDW are possible to be formed in the experiment. On the other hand, we enlarge the supercell of the $EuTe_4$ along ***a***- axis and ***b***- axis and fully relax the structures to find the possible CDW structures. We succeed in observing the ***a***-axial stripe CDW, whose energy is a little higher than the ***b***-axial stripe CDW (about 1.2 meV per atom), indicating the ***a***-axial stripe CDW as a meta-stable state.

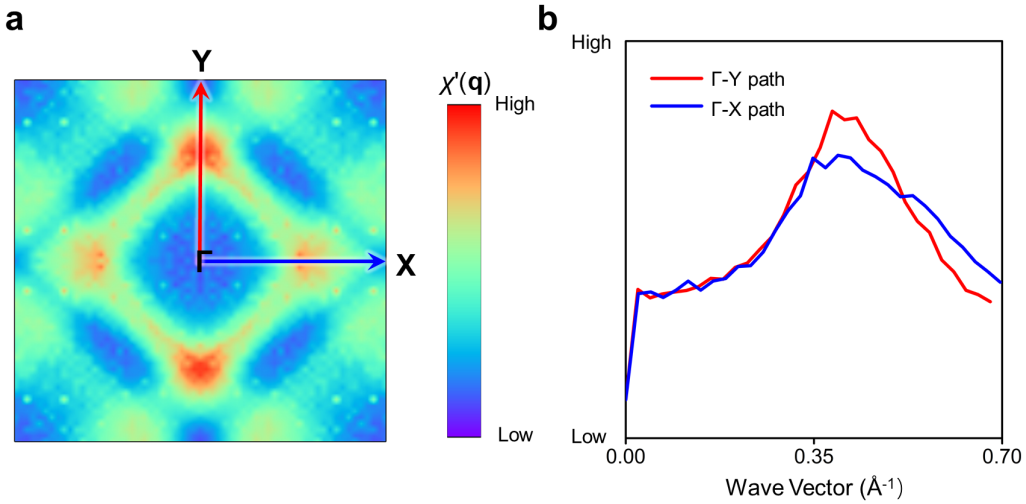

Fig. S12. Reasonable explanation for the 90° rotation of stripe CDW. (a) Lindhard functions of HT phase $EuTe_4$ before a stripe CDW. (b) Line profiles of (a) along two competing directions.

Supplementary Note 7: Bias Dependence of the Spindle-shaped Charge Order

Figure S13a-c show STM images of the spindle-shaped charge order taken on the same area using different bias voltages. Figure S13d-f are the corresponding FFT. It is shown that the intensity of $\boldsymbol{q}_1$' and $\boldsymbol{q}_2$' modulations varies significantly with the bias voltage, while the $\boldsymbol{q}_0$' modulation is always strong. This also indicates that $\boldsymbol{q}_1$' and $\boldsymbol{q}_2$' are not modulation wavevectors independent from $\boldsymbol{q}_0$', but are satellite peaks that come from the wavevector mixing effect.

Figure S14 exhibit the FFT images of bias-dependent differential conductance mappings of the spindle-shaped charge order. $\boldsymbol{q}_1$', $\boldsymbol{q}_2$', $\boldsymbol{q}_3$' and $\boldsymbol{q}_0$' show no frequency shift at different biases.

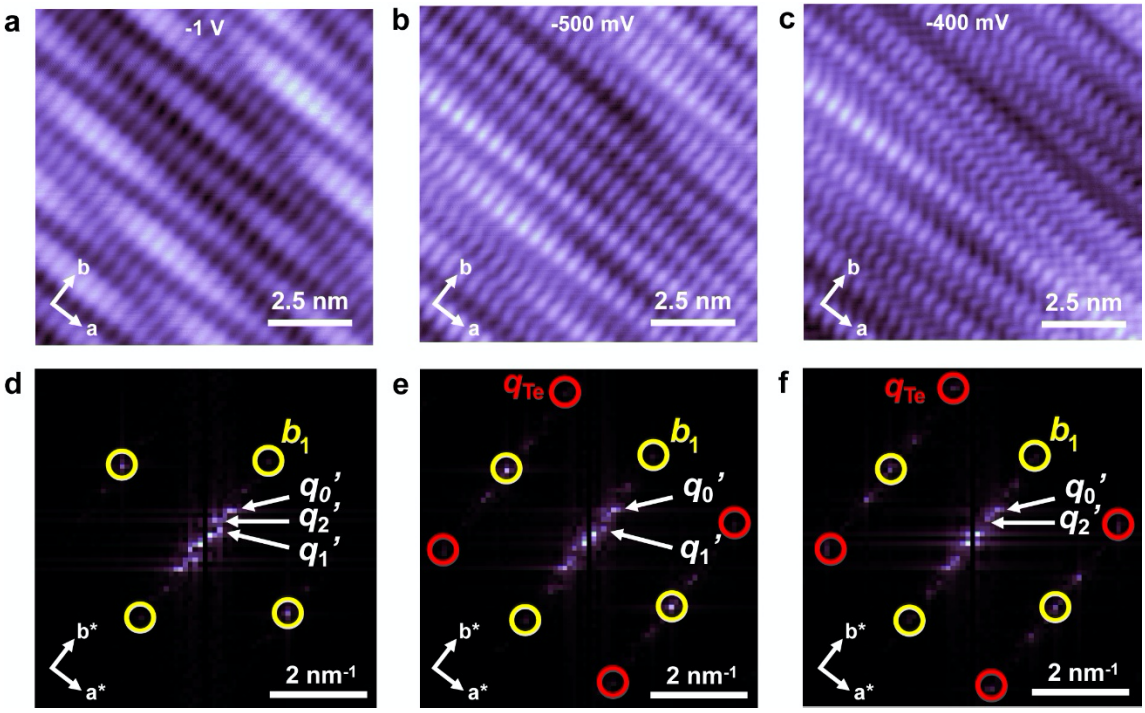

Fig. S13. Bias dependence of the spindle-shaped charge order. (a-c) STM topographic images taken on the same area with different bias voltages (at 4 K, 10 nm × 10 nm; V_b = -1000, -500 and -400 mV, respectively; I_t = 100 pA). (d-f) FFT of (a-c).

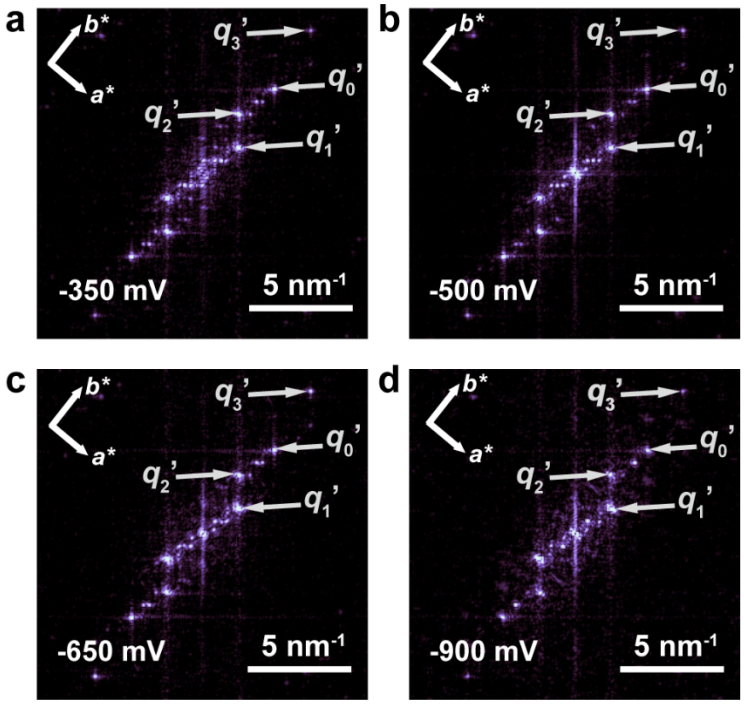

Fig. S14. FFT images of dI/dV mapping of the spindle-shaped charge order at different biases (at 4 K; set point: V_b = -1 V; I_t = 200 pA).

Supplementary Note 8: Rotation of the Spindle-shaped Charge Order

In the region where the stripe orientation rotates 90°, we also observed the spindle-shaped CDW (Fig. S15a). Fig. S15b is the FFT of Fig. S15a, clearly showing q_0' ~ q_3'. Since both stripe-like CDW and spindle-shaped CDW are observed in Fig. S15a, the signals in Fig. S15b are a superposition of q_0 ~ q_3 along the $\boldsymbol{a}^*$ axis and q_0' ~ q_3' slightly deviated from the $\boldsymbol{a}^*$ axis. Line-cuts of Fig. S15b along $\boldsymbol{a}_1$ and $\boldsymbol{b}_1$ directions also indicate that the stripe-like CDW is along the $\boldsymbol{a}^*$ axis (Fig. S15c). In Fig. S16, the calculated Lindhard functions of $\boldsymbol{a}$-axial stripe CDW show similar temperature-dependent $\boldsymbol{q}_{\text{off-axis}}$ as the $\boldsymbol{b}$-axial stripe-CDW (see Fig. 4f and Fig. S10). It indicates the spindle-shaped CDW can be formed within this $\boldsymbol{a}$-axial stripe CDW at low temperature, which is consistent with our observations.

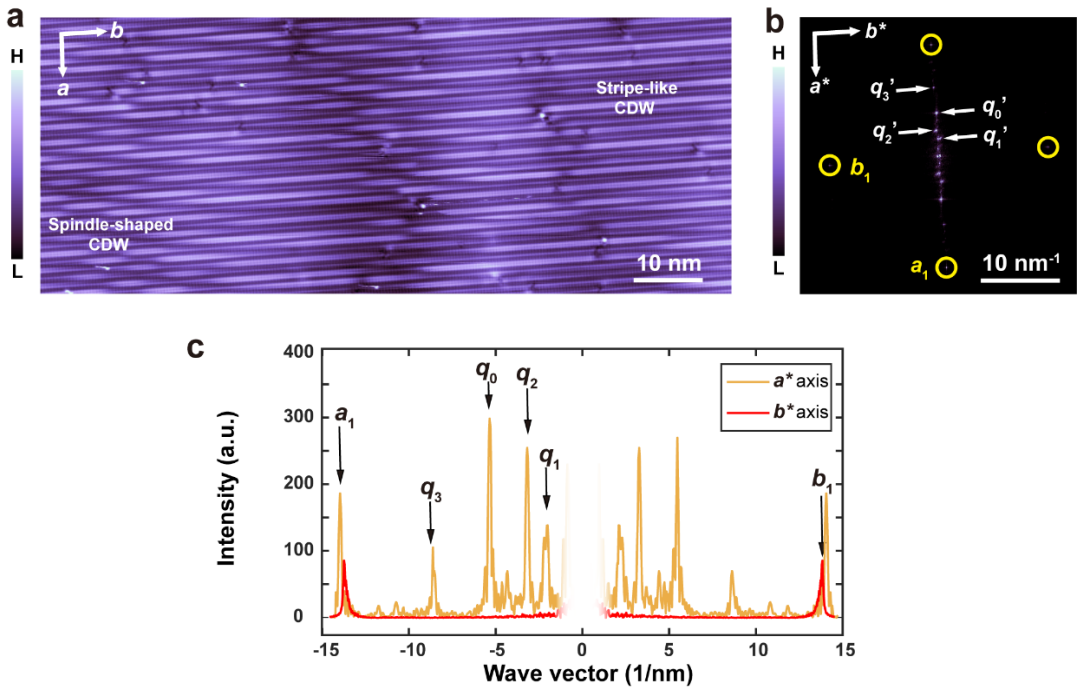

Fig. S15. (a) Spatial evolutions of the two types of charge orders in the $\boldsymbol{a}$-axial CDW region (100 nm × 40 nm, V_b = -900 mV, I_t = 50 pA). (b) FFT of (a). The wavevectors related with CDW is along the direction with smaller lattice constant ($\boldsymbol{a}^*$ axis). (c) Line-cuts of (b) along $\boldsymbol{a}_1$ and $\boldsymbol{b}_1$ directions.

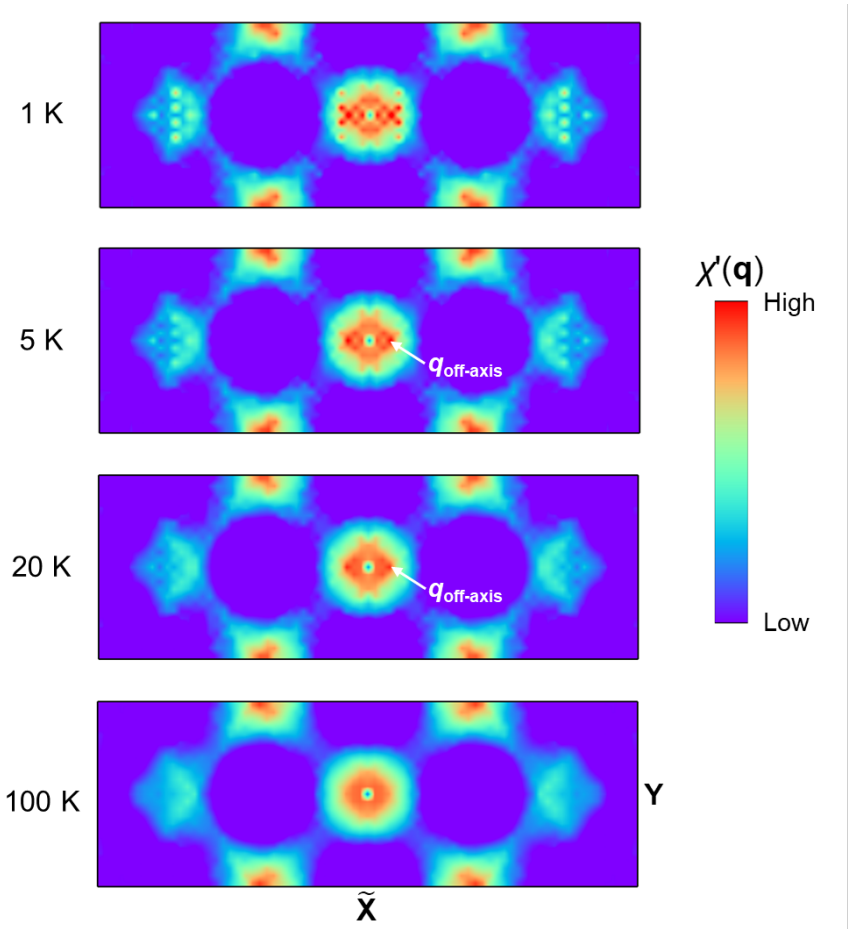

Fig. S16. Temperature-dependent Lindhard functions of $EuTe_4$ after forming the ***a***-axial stripe CDW.

Supplementary Note 9: The Stripe-like Charge Order at 77 K

Figure S17a and b show STM images of the stripe-like charge order taken at 77 K. Unlike at 4 K, the spindle-shaped patterns are rarely observed at 77 K. This phenomenon is consistent with previous XRD measurements that the CDW modulation is along the ***b*** axis within the temperature range from 30 K and 300 K.[6] It reveals the spindle-shaped CDW is unique at 4 K due to the suppression of stripe-like CDW.

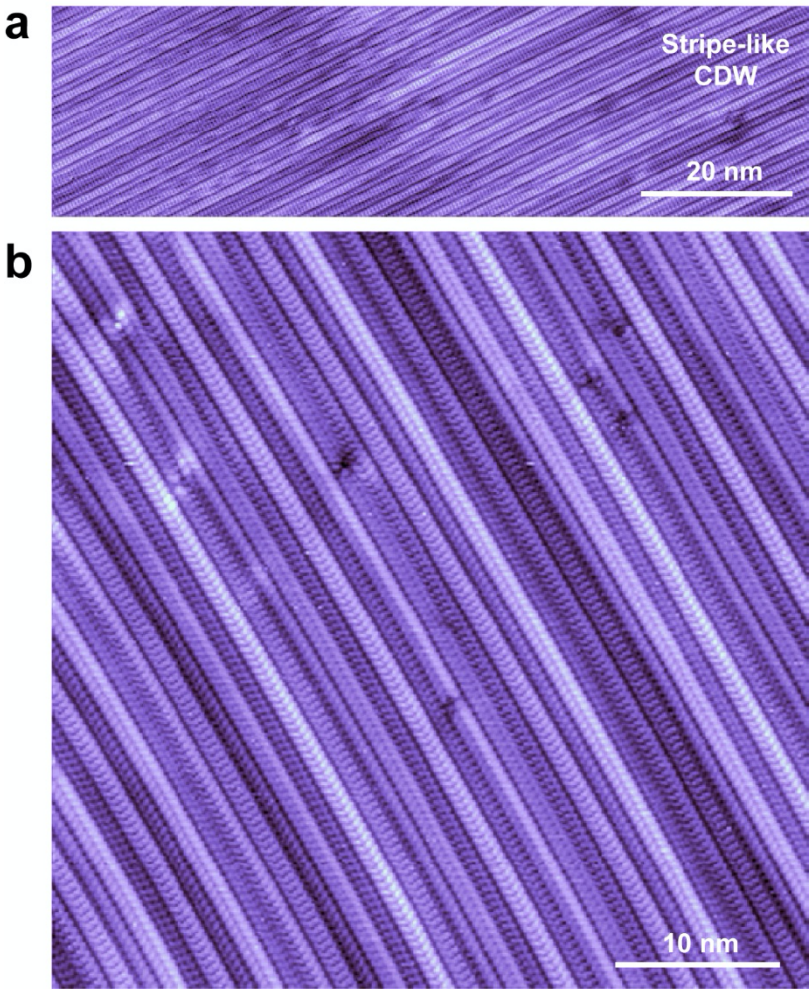

Fig. S17. STM topographic image taken at 77 K. (a) 100 nm × 28 nm; V_b = -1 V, I_t = 80 pA; (b) 46 nm × 46 nm; V_b = -1 V, I_t = 80 pA. The charge orders exhibit as the same as the stripe-like patterns observed at 4 K.

References

(1) Ru, N.; Condron, C. L.; Margulis, G. Y.; Shin, K. Y.; Laverock, J.; Dugdale, S. B.; Toney, M. F.; Fisher, I. R. Effect of chemical pressure on the charge density wave transition in rare-earth tritellurides RTe_3. *Phys. Rev. B* **2008**, *77* (3), 035114.
(2) Rathore, R.; Pathak, A.; Gupta, M. K.; Mittal, R.; Kulkarni, R.; Thamizhavel, A.; Singhal, H.; Said, A. H.; Bansal, D. Evolution of static charge density wave order, amplitude mode dynamics, and suppression of Kohn anomalies at the hysteretic transition in $EuTe_4$. *Phys. Rev. B* **2023**, *107* (2), 024101.
(3) Tomic, A. T. Scanning tunneling microscopy of complex electronic materials. *Ph.D. thesis, Michigan State University,* **2008**, Metrology SPIP, www.imagemet.com.

19A. Tomic, Ph.D. thesis, Michigan State University, 2008.
(4) Johannes, M. D.; Mazin, I. I. Fermi surface nesting and the origin of charge density waves in metals. *Physical Review B* **2008**, *77* (16), 165135.
(5) Pathak, A.; Gupta, M. K.; Mittal, R.; Bansal, D. Orbital- and atom-dependent linear dispersion across the Fermi level induces charge density wave instability in $EuTe_4$. *Physical Review B* **2022**, *105* (3), 035120.
(6) Zhang, C.; Wu, Q.-Y.; Yuan, Y.-H.; Zhang, X.; Liu, H.; Liu, Z.-T.; Zhang, H.-Y.; Song, J.-J.; Zhao, Y.-Z.; Wu, F.-Y.; et al. Angle-resolved photoemission spectroscopy study of charge density wave order in the layered semiconductor $EuTe_4$. *Phys. Rev. B* **2022**, *106* (20), L201108.